ChemComm

COMMUNICATION

View Article Online
View Journal

Cite this: DOI: 10.1039/d5cc03787e

Received 5th July 2025,
Accepted 22nd July 2025

DOI: 10.1039/d5cc03787e

rsc.li/chemcomm

K/Co co-doped carbon nitride nanocrystals for efficient hydrogen photosynthesis coupled with furfuryl alcohol oxidation

Yanmei Zheng,†[a] Xiaoli Liang,†[b] Ziwei Hang,[a] Jianghong Ouyang,[a] Jun Xing,[c] Xinli Guo*[b] and Zupeng Chen*[a]

K/Co co-doped carbon nitride (KCoCN) nanocrystals enable visible-light-driven H_2 evolution (550 μmol g^{-1} h^{-1}) coupled with furfuryl alcohol (FFA) oxidation to furoic acid (FA; 148 μmol and 89% conversion) without sacrificial agents. Mechanism studies reveal that KCoCN accelerates proton reduction to H_2 and promotes FFA oxidation to FA through a hole-driven radical mechanism.

Solar-driven photocatalytic water splitting offers a compelling route for clean H_2 generation.[1–3] Nonetheless, its widespread application is impeded by slow surface reaction kinetics, rapid recombination of photogenerated charge carriers, and the need for sacrificial agents, which often produce low-value or harmful by-products.[4,5] To overcome these limitations, coupling photocatalytic hydrogen production with biomass-derived alcohol oxidation presents a transformative approach. Biomass alcohols such as furfuryl alcohol (FFA) act as effective hole scavengers, contributing to enhanced H_2 evolution efficiency while simultaneously yielding high-value products like furoic acid (FA) through selective oxidation.[6] On the other hand, photogenerated electrons are used for water reduction to produce H_2, while holes drive the selective oxidation of alcohol molecules, which reduces the reaction energy barrier and solves the slow kinetics of the traditional water oxidation half-reaction.

Recently, the highly crystalline carbon nitride (CN) has attracted considerable attention due to its significantly improved bulk charge transfer and separation owing to reduced lattice scattering and a highly ordered structure.[7–9] However, the intrinsic poor carrier transport ability, anisotropic charge diffusion, and limited surface-active sites have hindered the efficiency of photocatalytic reactions.[8,10,11] CN nanocrystals have an excellent crystalline nanostructure, remarkable photostability, and orders of magnitude longer excited state lifetimes.[12,13] Moreover, nanocrystals' structure can transfer multiple electrons with minimal structural perturbation to provide sites for electron diffusion and accumulation.[14] Meanwhile, metal doping can increase the concentration of equilibrium majority carrier and electron trapping, thus modifying electrical properties and enhancing the conductivity.

Herein, we focused on the development of K/Co co-doped carbon nitride (KCoCN) nanocrystals for efficient hydrogen photosynthesis coupled with FFA oxidation. K^+ enhances interlayer spacing and active site exposure, while Co^{2+} introduces redox-active sites and promotes electron mobility. Fig. 1a and Fig. S1 show the preparation process of KCoCN nanocrystals. Typically, bulk CN is intercalated and exfoliated with HNO_3 to produce CN with a larger interlayer distance. Through molten salt treatment, K and Co ions can more easily enter the interlayers, forming K/Co co-doped CN (KCoCN) nanocrystals. Fig. S2a shows the scanning electron microscopy (SEM) image of bulk CN, which exhibits an irregular block structure formed by heavily stacked layers. As shown in Fig. S2b, with HNO_3 treatment, the layers of CN become more loosely packed due to the decomposition and gas release of the NO_3^- anions inserted between the layers, which successfully exfoliate the bulk CN layers. With the incorporation of K and Co ions, the surface of the catalyst becomes rough due to the etching effects of the metal ions (Fig. S3). Specifically, 5KCoCN (further defined as KCoCN unless otherwise specified) exhibits uniformly dispersed nanoparticles on its surface, which effectively increases the specific surface area and exposes more active sites. The transmission electron microscopy (TEM) image of KCoCN (Fig. 1b) shows that it is composed of high-density nanocrystalline clusters, which are attributed to the molten salt method providing

[a] National Key Laboratory for the Development and Utilization of Forest Food Resources, Jiangsu Co-Innovation Center of Efficient Processing and Utilization of Forest Resources, International Innovation Center for Forest Chemicals and Materials, College of Chemical Engineering, Nanjing Forestry University, Nanjing 210037, China. E-mail: czp@njfu.edu.cn

[b] Jiangsu Key Laboratory of Advanced Metallic Materials, School of Materials Science and Engineering, Southeast University, Nanjing, China. E-mail: guo.xinli@seu.edu.cn

[c] Key Laboratory of Eco-chemical Engineering, Ministry of Education, College of Chemistry and Molecular Engineering, Qingdao University of Science & Technology, Qingdao, 266042, China

† These authors contributed equally to this work.

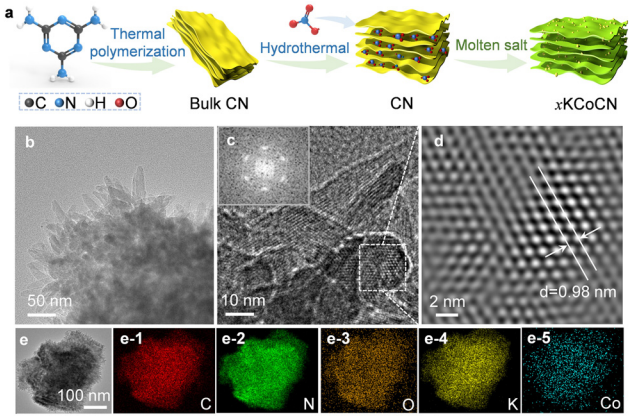

Fig. 1 (a) Schematic illustration showing the synthesis of KCoCN. (b) TEM image of KCoCN. (c) HRTEM image of KCoCN (the upper left inset shows the corresponding fast FFT image showing the good crystallinity of the sample). (d) The corresponding inverse IFFT image of KCoCN. (e) TEM images of KCoCN and the corresponding elemental mapping of C, N, O, K and Co.

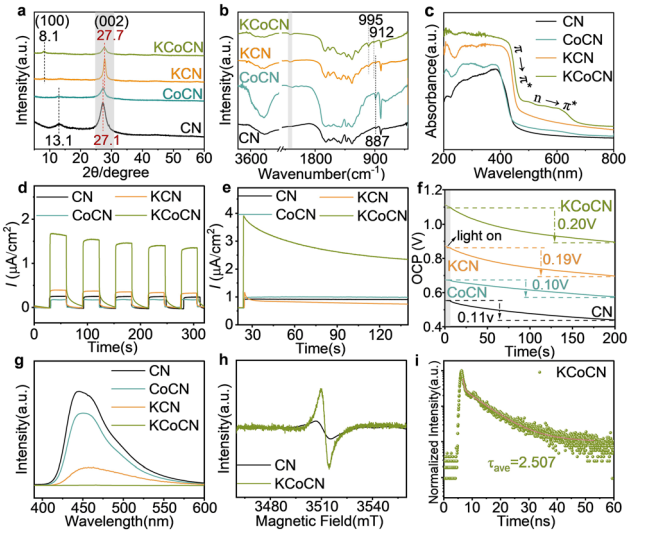

Fig. 2 (a) XRD patterns, (b) FT-IR spectra, (c) UV-Vis DRS spectra, (d) transient photocurrent, (e) long-term transient photocurrent curves, (f) open-circuit photovoltage (OCP), and (g) PL spectra (λ_{ex} = 355 nm) of CN, CoCN, KCN, and KCoCN. (h) EPR spectra of KCoCN and CN. (i) TPRL spectra of KCoCN.

an ionic liquid environment that enhances the diffusion and prevents the excessive aggregation of CN precursors at high temperatures. A high-resolution TEM (HRTEM) image shows that the as-grown polycrystalline KCoCN is linked by various orientation nanocrystals (Fig. 1c). The nanocrystal structure has remarkable photostability and transfers multiple electrons with minimal structural perturbation to provide sites for electron diffusion and accumulation. It demonstrates the corresponding fast Fourier transform (FFT) patterns in one single crystal domain, where the 6-fold rotational symmetric pattern suggests the hexagonal structure of KCoCN. In the inverse FFT (IFFT) image (Fig. 1d), the lattice distances are 0.98 nm, corresponding to the (100) planes of KCoCN. Fig. 1e shows the TEM images of KCoCN and the corresponding elemental distribution maps for C, N, O, K, and Co, which are evenly distributed across the entire sample, confirming the successful incorporation of K and Co into the CN structure. To further confirm the amount of Co incorporated into CN, ICP-MS analysis was performed. Table S1 shows that the Co content is 0.318%, further verifying the successful incorporation of Co. As shown in Fig. 2a, two significant diffraction peaks appear at 13.1° and 27.1° for CN and CoCN, corresponding to the (100) and (002) crystal planes, reflecting the triazine units' in-plane stacking and interlayer spacing.[15] With the introduction of K^+, the (100) peak shifts to 8.01° (Fig. S4a), indicating that the ordered in-plane structure is disrupted, which is attributed to Li^+ etching the in-plane structure of the heptazine unit to expand the periodic pore structure in KCoCN.[9] Additionally, the intensity of the (100) peak is significantly reduced because the metal ions have disrupted the ordered structure of CN.[16] Moreover, the intensity of the (002) peak decreases significantly after Co doping, suggesting that Co leads to local lattice expansion and the destruction of the periodic stacking. Fig. 2b and Fig. S4b show the FT-IR spectra. Compared to CN, a new peak appears at 2150 cm^{-1} in the KCoCN spectrum, corresponding to the vibration of the cyano group (–C≡N).[17] The formation of –C≡N can promote electron transfer and increase Lewis basic sites, thereby improving catalytic efficiency.[18] Additionally, a peak shifts from 887 cm^{-1} to a higher frequency at 912 cm^{-1} for the C stretching peak, indicating that CN interacts with Co(II) through N–Co coordination.[19] Furthermore, after K^+ doping, a new peak appears at 995 cm^{-1}, which is attributed to the symmetric vibration of metal–NC_2, and the intensity of this peak increases with the incorporation of Co, indicating the formation of K–N and Co–N electron bridges.[9] Further information on chemical compositions and surface oxidation states is displayed in XPS spectra (Fig. S5). After K and Co doping, the peak at 288.3 eV (C 1s spectra) shifts slightly to 288.6 eV, indicating that the doping of K and Co induces a change in the electronic environment.[20] In KCoCN, the N_{2C} and N_{3C} peaks display a slight redshift (398.8 → 399.0 eV), indicating that introducing K and Co changes the structure of CN and lowers the electron density. The K 2p high-resolution spectrum shows two peaks at 293.27 and 295.95 eV, corresponding to K $2p_{3/2}$ and K $2p_{1/2}$, respectively, confirming successful K-doping. The Co 2p spectrum reveals that Co is primarily present as Co^{2+}. Comparing CoCN with KCoCN, the Co peak in KCoCN shifts to a lower binding energy, indicating an increase in the electron density of Co. This suggests that after co-doping with K and Co, the electrons on CN are transferred to Co through Co–N bonds, making Co an electron-rich active site for photocatalytic reactions.

In UV-Vis diffuse reflectance spectroscopy (UV-Vis DRS), KCoCN exhibited stronger light absorption (Fig. 2c). Fig. S6 presents the corresponding $(\alpha h\nu)^{1/2} - h\nu$ curves, indicating that Co doping does not significantly affect the band gap of CN, whereas K doping leads to a noticeable reduction. The primary role of Co is to facilitate the n → π* electron transition (Fig. S7). The band structure (Fig. S8, measured from valence band (VB)-XPS[21,22]) indicates that the conduction band (CB) of KCoCN is positioned above the H_2 reduction potential, and its appropriate band gap facilitates efficient charge separation and migration, thus enhancing photocatalytic water splitting. In Fig. 2d and Fig. S9, the photocurrent density of 5KCoCN reaches

1.68 μA cm^{-2}, indicating that K and Co co-doping significantly enhances the separation efficiency of photogenerated carriers. Fig. S10 presents electrochemical impedance spectroscopy (EIS) data, suggesting that K/Co co-doping improves the conductivity of the material, enabling faster electron transfer to the reaction interface. Fig. S11 displays the linear sweep voltammetry (LSV) curves, which show that 5KCoCN exhibits the lowest onset potential, demonstrating easier electron migration and the highest current density at high potentials. In Fig. 2e and Fig. S12, 5KCoCN maintains a relatively high photocurrent density, demonstrating excellent carrier migration ability and stability against light corrosion. In Fig. 2f, KCoCN exhibits a higher photovoltage, which is favorable for enhancing the adsorption, decomposition, and reduction of reactants. As shown in the photoluminescence (PL) spectra (Fig. 2g and Fig. S13), the introduction of K and Co significantly suppresses the PL intensity, suggesting improved charge separation. Notably, as the Co content increases, the PL emission decreases dramatically and nearly vanishes, implying that Co doping may introduce structural defects that alter the electronic structure. This interpretation is supported by the electron paramagnetic resonance (EPR) spectra (Fig. 2h), which reveal a high density of nitrogen vacancies in KCoCN. Table S2 shows the decrease of the N/C ratio, further confirming the presence of nitrogen vacancies in KCoCN, which act as electron traps, reducing recombination and enhancing charge separation. The time-resolved fluorescence (TRFL) spectra were used to analyze the carrier lifetime (Fig. 2i and Fig. S14). Bi-exponential fitting revealed average carrier lifetimes of 4.892 ns for CN and 2.507 ns for KCoCN. The reduced lifetime in KCoCN implies enhanced non-radiative deactivation *via* charge transfer to localized states (*e.g.*, surface states), thereby facilitating more efficient charge separation.[23]

The photocatalytic performance for H_2 production and FFA oxidation was measured and the standard curves are shown in Fig. S15. As shown in Fig. S16, KCoCN exhibited the best catalytic activity, with 2.21 mmol g^{-1} of H_2 production and 0.59 mmol FA yield, which are higher than those of CN (0.03 mmol g^{-1} of H_2 and 0.05 mmol FA), KCN (1.37 mmol g^{-1} of H_2 and 0.33 mmol FA), and CoCN (1.03 mmol g^{-1} of H_2 and 0.22 mmol FA). As shown in Fig. 3a, KCoCN exhibits the best H_2 and FA production rates, indicating its high activity for H_2 production (550.48 μmol g^{-1} h^{-1}), and drives the oxidation of FA (0.148 mmol), demonstrating its excellent bifunctional catalytic ability. Moreover, the selectivity for FA and the conversion rate of FFA for KCoCN could reach 88.98% and 66.3%, respectively, as shown in Fig. 3b. This excellent performance could be attributed to the synergistic effect of K^+ (regulating the electronic structure to enhance the carrier separation) and Co^{2+} (providing active sites for oxidation) co-doping. As shown in Fig. S17, as the FFA concentration increases, the H_2 yield correspondingly increases, suggesting that FFA serves as a continuous hole scavenger, promoting carrier separation and enabling a synergistic enhancement of both oxidation and reduction reactions. Fig. 3c displays the time-dependent activity profile for the selective oxidation of FFA over 12 h. The

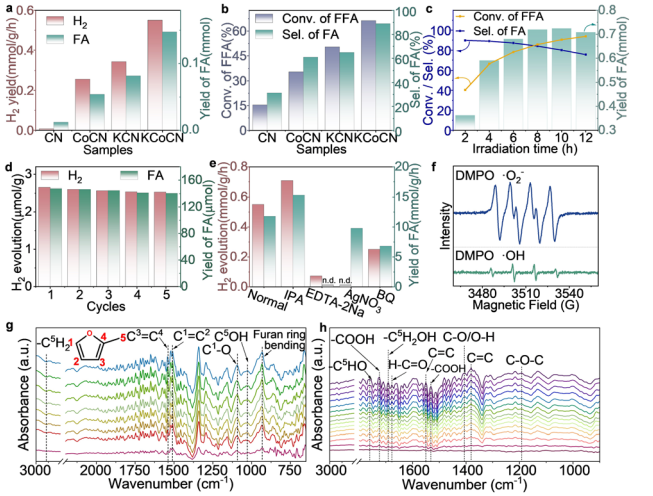

Fig. 3 (a) Comparison of H_2 and FA production rates ($\lambda \geq 420$ nm) and (b) selectivity for FA and the conversion rate of FFA. (c) Time-dependent activity profile for selective FFA oxidation within 12 h. (d) Cycling stability of H_2 and FA production. (e) Product yields on MACN in the presence of different scavengers. (f) The ERP spectra of DMPO $^{\bullet}O_2^-$ and $^{\bullet}$OH for KCoCN. *In situ* FT-IR spectra of Ni-BWO/CN for the adsorption of H_2O and FFA vapor (g) in the dark and (h) under light illumination with a 2-min time interval.

selectivity toward FA reached 75.5%, the FFA conversion rate reached 93.8%, and the H_2 production yield was 4.07 mmol g^{-1} (Fig. S18). Fig. 3d presents the long-term cycling stability of KCoCN under visible light conditions ($\lambda \geq 420$ nm), highlighting its durability and structural stability under reaction conditions. Fig. S19 shows the SEM images, XRD patterns, and FT-IR spectra of KCoCN before and after the recycling test. The unchanged results demonstrate that KCoCN possesses excellent structural stability and chemical durability, exhibiting strong potential for long-term applications.

To explore the mechanism of photocatalytic H_2 production coupled with FFA oxidation, an active species trapping experiment was conducted on KCoCN. When $AgNO_3$ and EDTA-2Na were added, the H_2 production process was significantly inhibited (Fig. 3e), indicating that holes and electrons are the main active species in the reaction. The FA yield is minimally affected by $AgNO_3$, suggesting that the oxidation of FFA to FA mainly relies on hole oxidation. Notably, the decrease in H_2 production and FA yield is attributed to the fact that $^{\bullet}O_2^-$ oxidizes the intermediate product FF to FA.[24–26] On the other hand, the addition of IPA led to a slight increase in H_2 production and FA yield, suggesting that the addition of IPA could prevent hydroxyl radicals ($^{\bullet}$OH) from further oxidizing FA.[25] Moreover, IPA reacts with holes to generate protons, promoting electron reduction to produce H_2. Correspondingly, KCoCN exhibits strengthened DMPO $^{\bullet}O_2^-$ and $^{\bullet}$OH spin-trapping electron paramagnetic resonance (EPR) signals (Fig. 3f), which further confirms the reaction pathway of KCoCN photocatalytic H_2 production and FFA oxidation. *In situ* FT-IR was utilized to investigate the photocatalytic oxidation of FFA to FA in depth. After adsorption equilibrium under dark conditions, the peaks at 1091, 1507, and 1571 cm^{-1} are ascribed to the vibration of C^1–O, C^1=C^2, and C^3=C^4 located on the furan ring (the order

of C is labeled in Fig. 3g).[4] The absorption peak at 2916 cm^{-1} is related to the asymmetric stretching vibration of methylene ($-C^5H_2$).[27] The infrared peak at 1028 cm^{-1} is assigned to the C^5OH of FFA.[28] The intensity of these peaks for FFA increased gradually, indicating the continuous adsorption of FFA. As the reaction proceeded (Fig. 3h), the stretching vibration of $-C^5H_2OH$ and $-C^5OH$ appeared at 1692 and 1795 cm^{-1}, verifying the conversion of FFA to FF.[29] Moreover, the gradually increased peaks at 1742, 1530, and 1406 cm^{-1} are assigned to –COOH in FA, indicating the formation of FA.[30]

Based on these results, the photocatalytic H_2 production coupled with FFA oxidation over KCoCN is illustrated in Fig. S20. The photogenerated electrons move to the surface to participate in water reduction reactions to produce H_2. The photogenerated holes are captured by FFA, driving its oxidation to high-value products FF and FA.

In conclusion, the optimized KCoCN exhibited excellent bifunctional catalytic activity, with a H_2 production rate of 550.48 μmol g^{-1} h^{-1} without a sacrificial agent. Simultaneously, it achieved a high FFA conversion rate (93.8%) and FA selectivity (75.5%). The enhanced performance is attributed to the synergy between K^+ and Co^{2+} doping, where K^+ ions regulate the electronic structure to enhance the carrier separation, while Co^{2+} introduces redox-active centers and cyano functionalities. Mechanism studies reveal that KCoCN nanocrystals effectively accelerate the reduction of protons to H_2 and promote the oxidation of FFA to FA through a hole-driven radical mechanism. This work offers new insights into the design of dual-function photocatalysts for solar energy utilization and biomass valorization.

Y. Zheng: data curation, formal analysis, investigation, and writing – original draft; X. Liang: data curation, formal analysis, investigation, and writing – original draft; Z. Hang and J. Ouyang: formal analysis and investigation; X. Guo and Z. Chen: supervision and writing – review & editing.

This work was supported by the National Key Research and Development Program of China (2023YFD2200505), the National Natural Science Foundation of China (22405127), and the Natural Science Foundation of Jiangsu Higher Education Institutions of China (21KJA150003).

Conflicts of interest

There are no conflicts to declare.

Data availability

Experimental procedures and the data supporting this article have been included as part of the SI.

Supplementary information is available. See DOI: **https://doi.org/10.1039/d5cc03787e**

Notes and references

1 Y. J. Cheng, J. Q. Zhao, X. F. Ma, H. L. Zheng, L. He, J. Zhang and Q. Lin, *Adv. Mater.*, 2025, 2503756.
2 Y. Yuan, J. Zhou, A. Bayles, H. Robatjazi, P. Nordlander and N. J. Halas, *Nat. Catal.*, 2024, **7**, 1339–1349.
3 Q. Wang, D. Zheng, Z. Pan, W. Xing, S. Wang, Y. Hou, M. Anpo and G. Zhang, *Adv. Funct. Mater.*, 2025, 2501889.
4 B. Liu, Y. Li, Y. Guo, Y. Tang, C. Wang, Y. Sun, X. Tan, Z. Hu and T. Yu, *ACS Nano*, 2024, **18**, 17939–17949.
5 X. Du, H. Ji, Y. Xu, S. Du, Z. Feng, B. Dong, R. Wang and F. Zhang, *Nat. Commun.*, 2025, **16**, 3024.
6 J. Hu, X. Li, J. Qu, X. Yang, Y. Cai, T. Yang, F. Yang and C. M. Li, *Chem. Eng. J.*, 2023, **453**, 139957.
7 D. S. Zhang, Q. Gao, Z. Chang, X. T. Liu, B. Zhao, Z. H. Xuan, T. L. Hu, Y. H. Zhang, J. Zhu and X. H. Bu, *Adv. Mater.*, 2018, **30**, e1804715.
8 J. Li, Y. Li, S. Wei, S. Wu, Z. Peng, F. Zhang, L. Huang, L. Chen, J. Li and H. Xiao, *Appl. Catal., B*, 2025, **366**, 125073.
9 Y. Zheng, Y. Cui, Q. Ruan, Y. Zhao, H. Hou, Y. Zhou, C. Ling, J. Wang, Z. Chen and X. Guo, *ACS Nano*, 2024, **18**, 14583–14594.
10 H. Jiang, W. Ye, H. Zhen, X. Luo, V. Fominski, L. Ye and P. Chen, *Chin. Chem. Lett.*, 2025, **36**, 109984.
11 W. Yu, R. Xing, N. Tian, Y. Wang, N. Zhang, Y. Zhang, Y. Deng and H. Huang, *J. Mater. Chem. A*, 2025, **13**, 3791–3801.
12 Octavi E. Semonin, Joseph M. Luther, Sukgeun Choi, Hsiang-Yu Chen, Jianbo Gao, Arthur J. Nozik and M. C. Beard, *Science*, 2011, **334**, 1530–1533.
13 M. P. Boneschanscher, W. H. Evers, J. J. Geuchies, T. Altantzis, B. Goris, F. T. Rabouw, S. A. P. van Rossum, H. S. J. van der Zant, L. D. A. Siebbeles, G. Van Tendeloo, J. H. I. Swart, A. V. Petukhov and D. V. S. Bals, *et al.*, *Science*, 2014, **344**, 1377–1380.
14 W. A. Tisdale, K. J. Williams, B. A. Timp, D. J. Norris, E. S. Aydil and X.-Y. Zhu, *Science*, 2010, **328**, 1543–1547.
15 J. Qu, Y. Zhang, X. Liang, Y. Zheng, Y. Li, J. Ren and X. Guo, *Sep. Purif. Technol.*, 2025, **359**, 130813.
16 J. Gao, Y. Wang, S. Zhou, W. Lin and Y. Kong, *ChemCatChem*, 2017, **9**, 1708–1715.
17 X. Wu, X. Wang, F. Wang and H. Yu, *Appl. Catal., B*, 2019, **247**, 70–77.
18 F. Guo, B. Hu, C. Yang, J. Zhang, Y. Hou and X. Wang, *Adv. Mater.*, 2021, **33**, 2101466.
19 A. Rubab, N. Baig, M. Sher, M. Ali, A. Ul-Hamid, N. Jabeen, L. U. Khan and M. Sohail, *ChemNanoMat*, 2022, **8**, 2100428.
20 Y. Li, L. Ding, Y. Guo, Z. Liang, H. Cui and J. Tian, *ACS Appl. Mater. Interfaces*, 2019, **11**, 41440–41447.
21 R. You, H. Dou, L. Chen, S. Zheng and Y. Zhang, *RSC Adv.*, 2017, **7**, 15842–15850.
22 X. Li, B. Kang, F. Dong, Z. Zhang, X. Luo, L. Han, J. Huang, Z. Feng, Z. Chen, J. Xu, B. Peng and Z. L. Wang, *Nano Energy*, 2021, **81**, 105671.
23 Z. Chen, A. Savateev, S. Pronkin, V. Papaefthimiou, C. Wolff, M. G. Willinger, E. Willinger, D. Neher, M. Antonietti and D. Dontsova, *Adv. Mater.*, 2017, **29**, 1700555.
24 Q. Xue, H. Li, P. Jin, X. Zhou and F. Wang, *Angew. Chem., Int. Ed.*, 2025, e202423368, DOI: **10.1002/anie.202423368**.
25 W. Liang, G. Xu and Y. Fu, *Appl. Catal., B*, 2024, **340**, 123220.
26 H. Wang, L. Liu, J. Bian and C. Li, *J. Fuel Chem. Technol.*, 2024, **52**, 1617–1628.
27 Y. Tang, Y. Guo, B. Liu, Y. Li, Z. Hu, X. Tan, J. Ye and T. Yu, *Adv. Energy Mater.*, 2025, 2501159.
28 Q. Li, X. Li, M. Zheng, F. Luo, L. Zhang, B. Zhang and B. Jiang, *Adv. Funct. Mater.*, 2024, **35**, 2417279.
29 J. Yu, Y. Yang, L. Chen, Z. Li, W. Liu, E. Xu, Y. Zhang, S. Hong, X. Zhang and M. Wei, *Appl. Catal., B*, 2020, **277**, 119273.
30 S. Si, P. Gong, X. Bao, X. Tan, Y. Mao, H. Zhang, D. Xiao, K. Song, Z. Wang, P. Wang, Y. Liu, Z. Zheng, Y. Dai, B. Huang and H. Cheng, *ACS Catal.*, 2024, **14**, 8343–8352.

